Infrared free electron laser induced photodesorption of CO and N_2 from solid amorphous water at cryogenic temperatures

Kerry H. Jones[1], Jack E. Fulker*[,2], Domantas Laurinavicius[3], Ali Ozel[3], J. G. M. Schrauwen[4], Britta Redlich[4], Jennifer A. Noble[2], Sergio Ioppolo[5], Martin R. S. McCoustra[3], and Wendy A. Brown*[,1]

[1]Department of Chemistry, University of Sussex, Falmer, Brighton, BN1 9QJ, UK

[2]Physique des Interactions Ioniques et Moléculaires (PIIM): CNRS, Aix-Marseille Université, Marseille, France

[3]School of Engineering and Physical Sciences, Heriot-Watt University, Edinburgh, EH14 4AS, Scotland

[4]HFML-FELIX laboratory, Radboud University, Nijmegen 6525 ED, The Netherlands

[5]Department of Physics and Astronomy, University of Aarhus, Ny Munkegade 120, 8000 Aarhus C, Denmark

Supplementary Information

RAIR Spectra of Unirradiated CO and N_2 water ice mixtures

Figure S1 shows a close up of the wavenumber region between 3500 – 3900 cm^{-1} of Figure 2 in the main article. The weak absorption features observed are characteristic of dangling OH (dOH) modes present at the ASW vacuum interface. These features arise due to water molecules that are not tetrahedrally bound to neighbouring water molecules and so become blue-shifted relative to the broad OH stretching feature at ~3 μm. Figure S1a shows that for a pure ASW ice, two distinct dOH features arise, at ~3696 cm^{-1} (~2.71 μm) and ~3721 cm^{-1} (~2.69 μm). These are assigned to the 3- and 2-coordinated water sites on the ASW surface, respectively.[1-4] Figure S1b shows the disappearance of the two dOH features in a 14% CO:H_2O mixed ice. This is due to relatively strong electrostatic binding between CO and the dangling H atoms at the ASW surface, leading to red-shifting of the dOH absorption modes into the bulk O-H stretch band. He *et al.*[5] reported similar results for the co-deposition of a CO:H_2O ice (30 ML CO in 100 ML H_2O) at 10 K, observing not only the shifting of the dOH modes, but also the emergence of a weak, broad absorption feature at 3635 cm^{-1} which we do not observe in these experiments.

The inset to Figure S1b show two peaks at ~2137 and ~2152 cm^{-1}, corresponding to the CO compact-/π- and extended-/σ-interacting configurations within ASW ice pores respectively.[6] We adopt this assignment from the work of Collings *et al.*[6,7] as studies by He *et al.*[8] indicate that the pore surface area of 200 L_m of ASW is equivalent to more than 40 L_m of CO. Hence

our mixtures are likely to consist of a CO monolayer dispersed on the pore surfaces of the porous ASW matrix. This interpretation, *i.e.*, the shifting of dOH modes alongside the growth of the 2152 cm^{-1} band due to CO directly interacting with dOH modes, is also consistent with the tendency of CO molecules to preferentially occupy dOH sites over non-dOH sites. Several studies of CO adsorption on ASW surfaces report a sharp feature at 2143 cm^{-1}, attributed to multilayer CO growth once the pores are saturated.[7-10] This behaviour contrasts with the band profile observed here, further supporting the assignment of the ~2139 cm^{-1} feature to CO–CO interactions within ASW pores in the ice mixture, while the ~2152 cm^{-1} band arises from CO–dOH interactions at the pore interface. These interactions are illustrated in Figure S1.

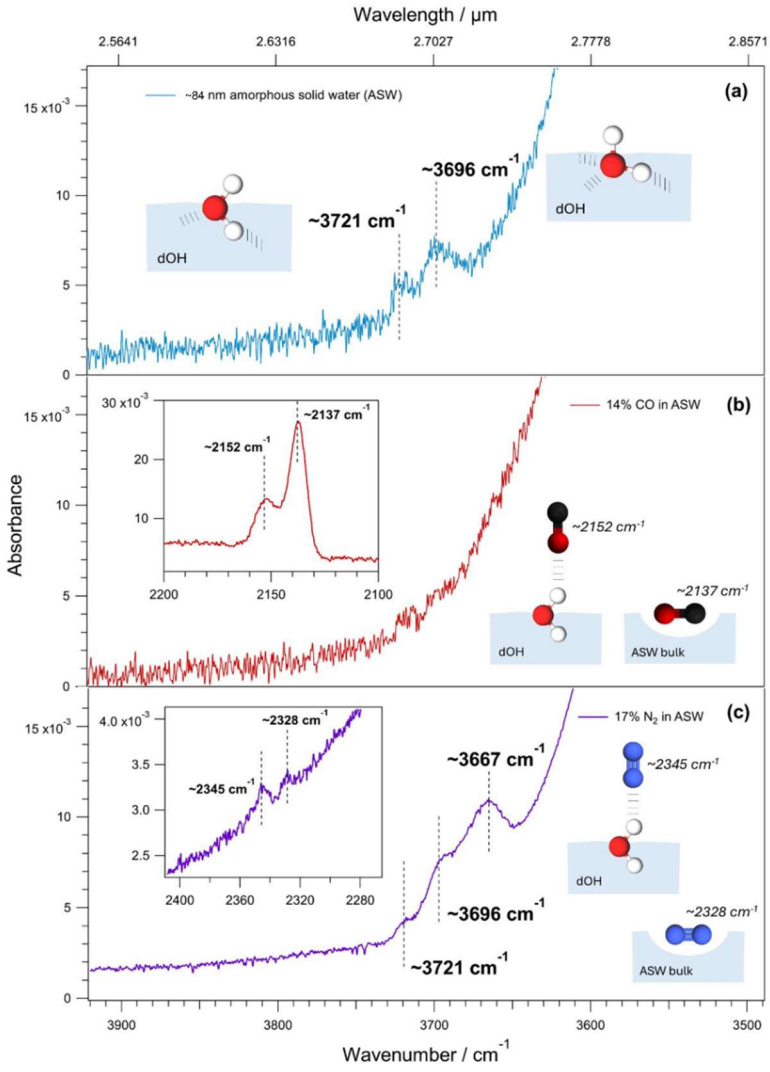

Figure S1: RAIR spectra showing the dangling OH (d-OH) mode region from Figure 2 of (a) amorphous solid water deposited at 9 K; (b) a 14% CO:H_2O mixture deposited at 9 K; and (c) a 17% N_2:H_2O mixture deposited at 9 K. Cartoons show the orientation of the surface dOH modes of ASW in (a), and possible interactions between dOH modes and within the pores of ASW with either CO in (b) or N_2 in (c). The spectra in (a) and (b) were taken with a standard acquisition of 256 scans, whereas the spectrum in (c) was taken with a longer acquisition of 512 scans to better resolve the N_2 features at 2345 cm^{-1} and 2328 cm^{-1}.

In contrast to the behaviour of CO, N_2 does not preferentially bind to dangling OH groups, according to a study by Zubkov *et al*.[11] This explains why, in Figure S1c, the ~3696 and ~3721 cm^{-1} dOH features are unaffected in the N_2:H_2O ice mixture. Instead, a third feature appears at ~3667 cm^{-1}. This suggests that N_2 induces a perturbation in the dOH and facilitates the formation of a new dOH–N_2 environment, but does not shift the dOH vibrations in the same way as CO. This discrepancy arises from the differences in polarity and binding strength of the two species. He *et al.*[5] report only two dOH features for a N_2:H_2O ice (30 ML N_2 in 100 ML H_2O) co-deposited at 10 K, at 3668 and 3692 cm^{-1}, where the 3 coordinated dOH peak is shifted by ~28 cm^{-1}. In contrast, CO shifts this peak by ~61 cm^{-1}.

While the N-N stretch of N_2 is formally IR forbidden by symmetry in the gas phase, it is known that in the condensed phase, symmetry breaking *via* intermolecular interactions can occur, thus weakly allowing the vibration.[12-14] Indeed, the N-N stretch has been reported at 2328 cm^{-1} in solid N_2.[13] Observations of N-N stretching modes are easier using Raman spectroscopy as the mode is Raman allowed, and a feature is observed at around 2324 cm^{-1} in nitrogen clathrate hydrates.[15] Computational studies report dimer cluster structures not unlike those of CO-H_2O dimers with extended and compact forms.[16] These studies report weak IR active modes for N_2 in the range 2352.6 cm^{-1} – 2359.3 cm^{-1} subject to the exact cluster geometry.

The inset in Figure S1c shows the spectral window in which the N-N stretch occurs. In considering the literature above, the low frequency mode at ~2328 cm^{-1} is assigned to a mode equivalent to that observed in nitrogen clathrate hydrates (a more compact complex with the N_2 interacting with more than one H_2O). The higher frequency band at 2345 cm^{-1} is not inconsistent with N_2 in an extended geometry structure like the dimer mode at 2359.3 cm^{-1}. However, gas phase CO_2 in the purge gas for the IR optics cannot be completely excluded as it also appears in this wavenumber range.

Laser Heating Simulations: Two-temperature model

The two-temperature mathematical model proposed by Anisimov *et al.*[17] is commonly applied to describe the highly non-equilibrium processes induced by ultrafast laser excitation. This is a phenomenological model, where the temporal evolution of the energy of the electron and lattice reservoirs as well as the transfer of energy between these systems are resolved. The two-temperature model is used to simulate a broad range of experiments in the ultrafast community, *e.g.*,[18,19].

The energy balance equations for electron and lattice reservoirs are given as:

$$c_{pe,i}(T_{e,i})\rho_i \frac{\partial T_{e,i}}{\partial t} = \frac{\partial}{\partial x} k_{e,i}(T_{e,i}) \frac{\partial T_{e,i}}{\partial x} + G_{e\leftrightarrow p}(T_{l,i} - T_{e,i}) + S(x,t) \quad \text{(E1)}$$

$$c_{pl,i}(T_{l,i})\rho_i \frac{\partial T_{l,i}}{\partial t} = \frac{\partial}{\partial x} k_{l,i}(T_{l,i}) \frac{\partial T_{l,i}}{\partial x} + G_{e\leftrightarrow p}(T_{e,i} - T_{l,i}) \quad \text{(E2)}$$

Here, for the *i*th material, ρ_i is the mass density, $T_{e,i}$ and $T_{l,i}$ are electron and lattice temperatures, $c_{pe,i}$ and $c_{pl,i}$ are electron and lattice heat capacity, $k_{e,i}$ and $k_{l,i}$ are electron and lattices thermal conductivities, $\mathrm{G_{e\leftrightarrow p}}$ is the energy exchange coupling factor between electron and lattice, and $S(x,t)$ is the energy source to the electronic reservoir due to the laser heating. Using NTMpy[20], the equations (E1) and (E2) are solved in one dimension across the layered media. Temperatures are expanded as linear combinations of splines which converts the partial differential equation system into a finite-dimensional form expressed in terms of coefficient vectors. Derivatives are computed analytically at collocation points *via* spline matrices. Temporal evolution is obtained using the explicit Euler method, with automatic time-step selection based on eigenvalue stability analysis of the system's dynamical matrix.

Laser Heating Simulations: Simulation Configurations

Figure 1 of the main article shows the schematic of the pulsed laser structure of the FEL-2 laser light source at the FELIX facility. For our simulations, we match the experimental conditions and use a macropulse with a duration of approximately 6 μs. The micropulses had a full width at half maximum (FWHM) of 4 ps, and each macropulse contained 6000 micropulses (with a temporal spacing of 1 ns). The total energy deposition was chosen to be 40 mJ. The laser's spot areas are 0.00059 and 0.00437 cm^2 for 3 and 4.7 μm wavelengths, respectively.

We are considering [Au|Cu] and [Ice|Au|Cu] material stacks for 1D simulations. The physical properties and modelling constants of ice, gold and copper are given in Table S1. The following assumptions are applied: i) there is no data available for electron and lattice heat conductivities for ice at very low temperature, therefore, interpolated data were used, ii) the coupling term, $G_{e\leftrightarrow p}$, is assumed to not be a function of temperature. However, recent studies, ***e.g.***, [21], discuss its dependency on the temperature. iii) lattice heat conductivities at low temperature for ice, gold and copper are not available, therefore, they were assumed to be equal to the electron heat conductivities.

Table S1: Physical properties of Ice-Au-Cu stack.

Parameter	Ice	Gold	Copper
Density (ρ_i) / $\mathrm{kg\,m^{-3}}$	1040	19320	8960
Thickness (l) / nm	60	100	3175× 10^3
Refractive index (n) / –	1.3325+0.0157j	1.4684+1.9530j	1.3135+2.1309j
Electron heat conductivity ($k_{e,i}$) / $\mathrm{W\,m^{-1}K^{-1}}$	$0.06T_e$	$0.0457047T_e$ [22]	$0.0734766T_e$ [22]
Lattice heat conductivity ($k_{l,i}$) /$\mathrm{W\,m^{-1}K^{-1}}$	$k_{e,i}$	$k_{e,i}$	$k_{e,i}$
Electron heat capacity ($c_{pe,i}$) / $\mathrm{J\,kg^{-1}K^{-1}}$	$0.0075T_e$ [24]	$0.003264T_e$ [22]	$0.007949T_e$ [22]
Lattice heat capacity ($c_{pl,i}$) / $\mathrm{J\,kg^{-1}K^{-1}}$	$c_{pe,i}$	4.758433 $\times 10^{-5}T_e$ [23]	1.2244 $\times 10^{-5}T_e$ [23]
Electron phonon coupling ($G_{e\leftrightarrow p}$) / $\mathrm{Wm^{-3}K^{-1}}$	10^{16}	6.089×10^{16} [22]	3.95×10^{16} [22]

Laser Heating Simulations: Results and Discussion

Clean Surface: Au-Cu

We first validated the mathematical and computational modelling framework through temperature evolution measured by a thermocouple. A schematic of the 1D layer stack model imposed onto the Au-coated Cu sample is shown in Figure S2.

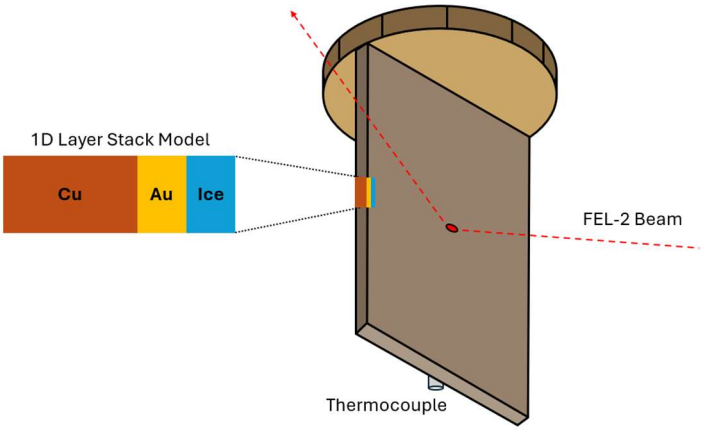

Figure S2: Schematic of how the thermocouple setting on the copper substrate relates to the 1D layer stack model used in the laser heating simulations.

As the thermocouple could not provide the spatial resolution of temperature along the layers, we averaged the predicted temperature along layers. Figure S3a shows the temporal evolution of the measured temperature for one minute of laser heating. The temperature shows a sudden increase from 10.06 to 10.18 K during the early stage of the heating and it oscillates around 10.18 K in the later stage. Figure S3b shows the temporal evolution of the predicted lattice temperature for a macropulse duration. The computational study is limited to have a femtosecond timestep, therefore it is not feasible to perform a simulation for a duration of 1 minute. The predicted temperature at the end the 1st macropulse is 10.35 K, which is in reasonable agreement with the experimental data. This discrepancy might come from the laser pulse energy whose uncertainty is 10 mJ. The inset of Figure S3b shows the evolution of the electron and lattice temperatures for the first 5 micropulses, which shows a cooling stage just after a micropulse. One can also see from the near-overlapping trends that the difference between electron and lattice temperatures is negligible.

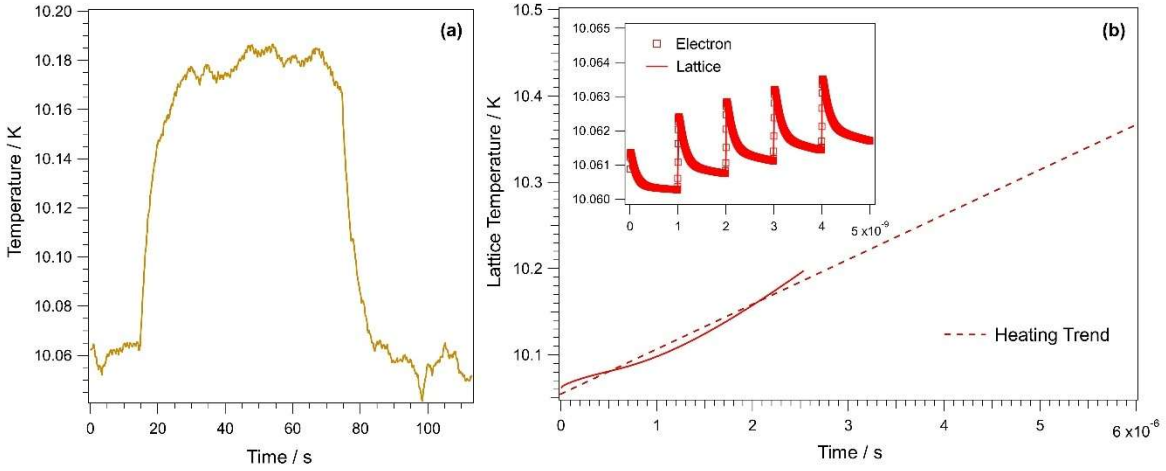

Figure S3: The Au-Cu case; (a) Temporal evolution of the measured temperature for a minute of laser heating. (b) Temporal evolution of the predicted lattice temperature for a macropulse duration of 6 μs. (b-Inset) Evolution of electron and lattice temperatures for the first 5 micropulses (electron and lattice temperature profiles are overlapping).

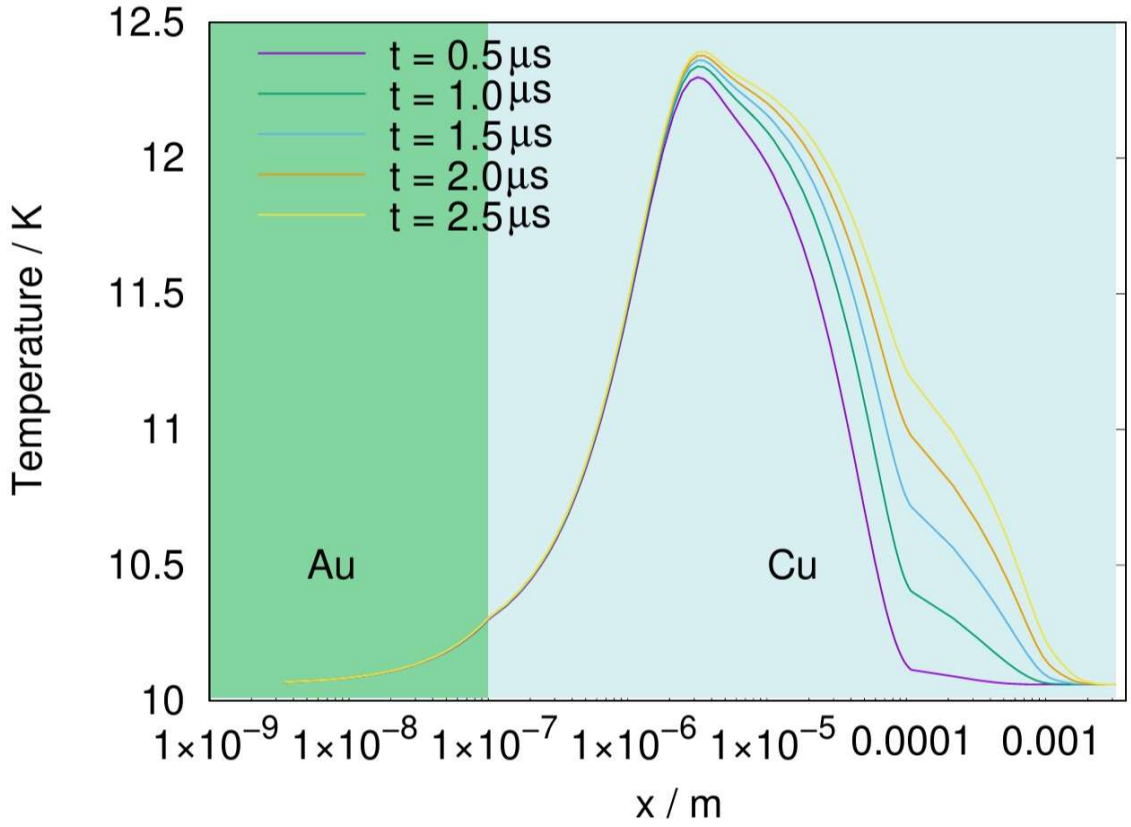

Figure S4: The Au-Cu case; Spatial evolution of predicted temperature at time instants of 0.5, 1.0, 1.5, 2.0 and 2.5 μs.

Figure S4 shows the spatial evolution of the predicted lattice temperature at time instants of 0.5, 1.0, 1.5, 2.0 and 2.5 μs. Au and Cu regions are shaded with light green and blue, respectively. The highest temperature around ~12.3 K occurs in the Cu substrate and not at the gold surface. Indeed, the gold surface appears to remain close to the base temperature of the system. This reflects stronger coupling of the IR radiation field into the Cu than the Au and suggests that laser-induced thermal desorption is unlikely to occur at the gold surface.

Ice-Au-Cu case:

Figure S5a shows the evolution of measured temperature for the ice-gold-copper stack. In comparison to the Au-Cu case, the temperature jump is larger at ~0.6 K. The predicted temperature is around 9.45 K (Figure S5b), which is in reasonable agreement with the experimental data.

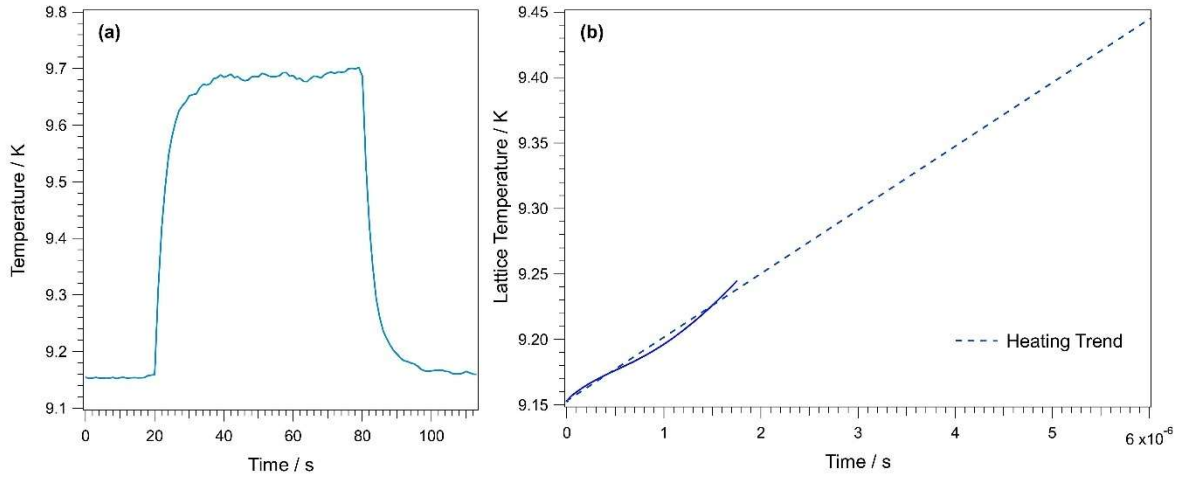

Figure S5: The Ice-Au-Cu case; (a) Temporal evolution of measured temperature for a minute laser heating. (b) Temporal evolution of predicted lattice temperature for a macropulse duration of μs.

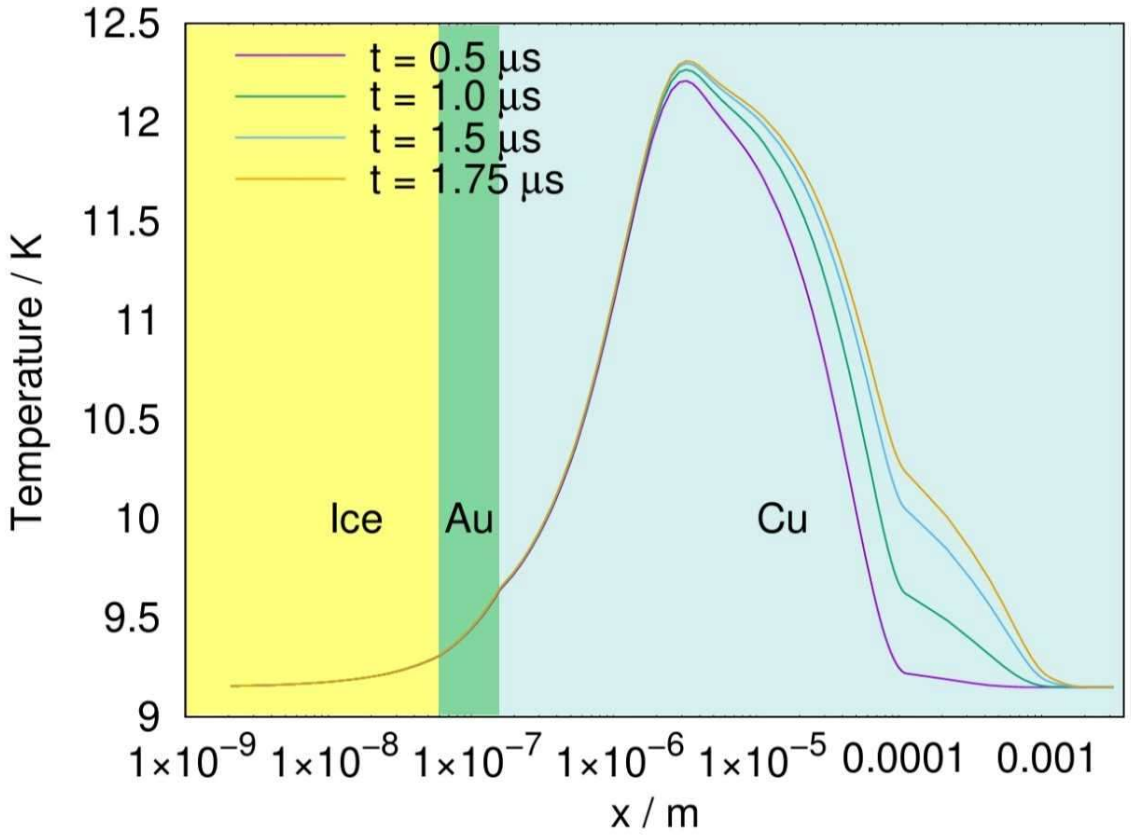

Figure S6: The Ice-Au-Cu case; Spatial evolution of predicted temperature at time instants of 0.5, 1.0, 1.5 and 1.75 μs.

Figure S6 shows the spatial evolution of the predicted lattice temperature at time instants of 0.5, 1.0, 1.5 and 1.75 μs. Again, the highest temperature around ~12.3 K occurs in the Cu substrate and not at the ice or gold surfaces. Indeed, these surfaces appear to remain close to the base temperature of the system. This suggests that laser-induced thermal desorption is unlikely to occur at the ice surface.

Photon-Induced Desorption Behaviour

The semi-logarithmic plot in Figure S7 demonstrates that the natural decay of the peak PID signal from a typical irradiation of a CO:H_2O ice cannot be adequately described by a single-exponential function and is therefore better represented by a bi-exponential fit.

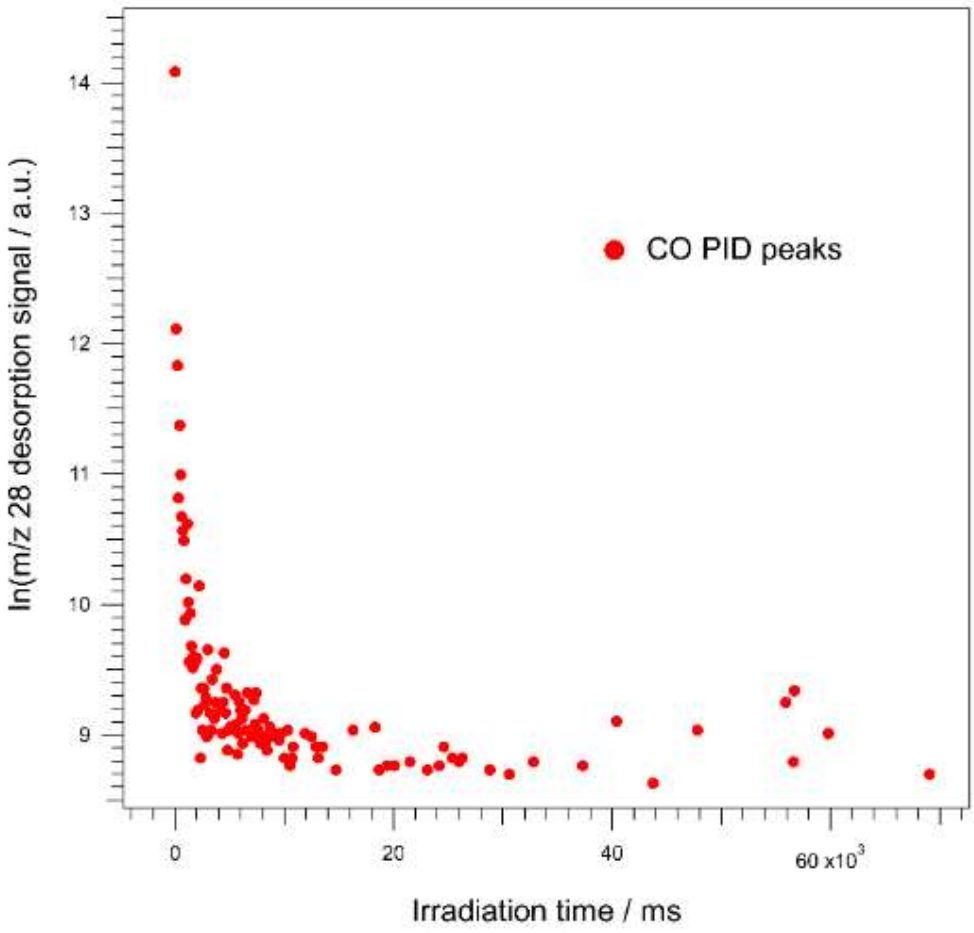

Figure S7: The natural log of the peak transient values of the PID data for a 1-minute irradiation of a 11% CO:H_2O mixed ice at a wavelength of 3 μm with an energy of 36 ± 5 mJ *vs.* irradiation time. The natural curve of the data highlights the need to treat the data with a bi-exponential fit.

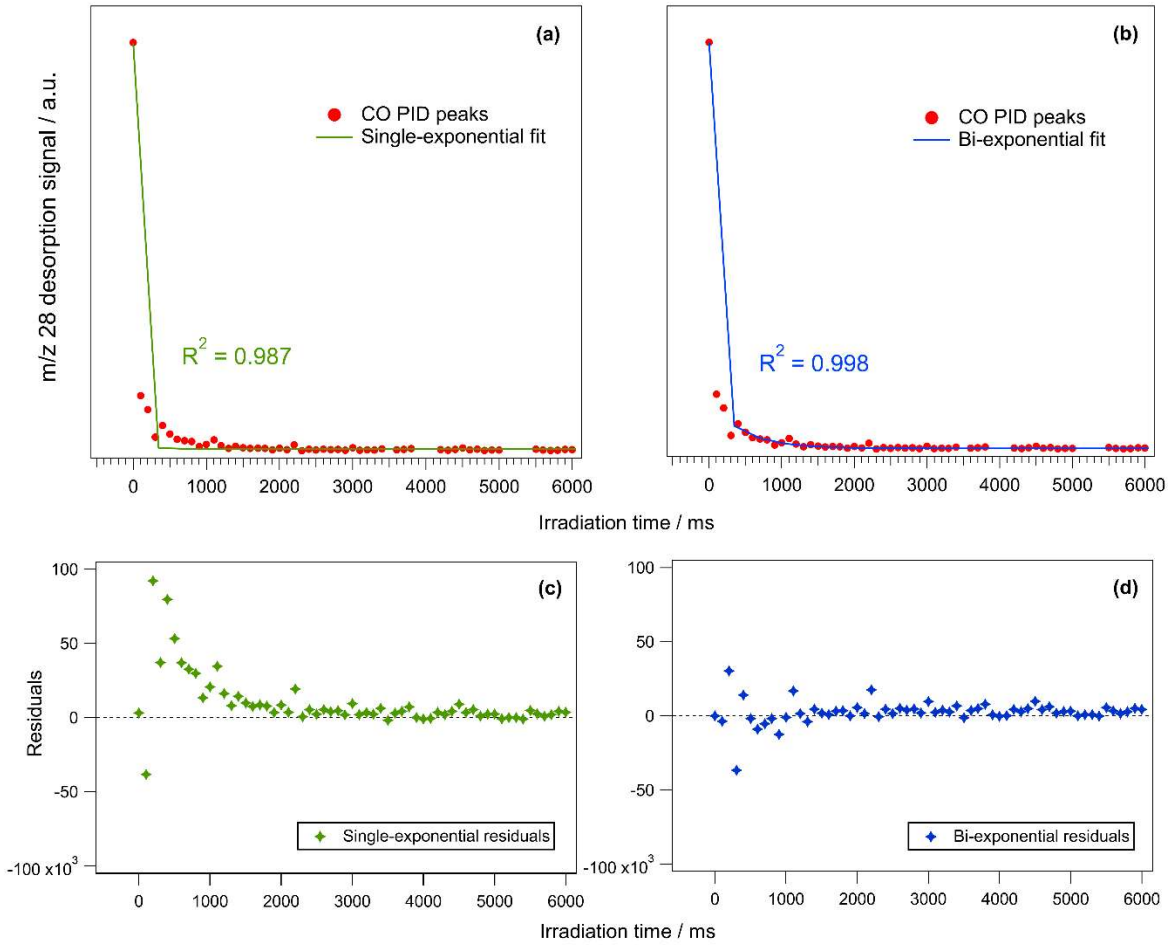

Figure S8: Example PID traces for the data resulting from a 1-minute irradiation of an 11% CO:H_2O mixed ice at a wavelength of 3 μm with an energy of 36 ± 5 mJ, fitted with (a) a single-exponential function and (b) a bi-exponential function. The plots preview the first 6 s of the 1-minute irradiation only. The residuals as a function of irradiation time are plotted for the (c) single-exponential and (d) bi-exponential fits.

Figure S8 compares single-exponential and bi-exponential fits (panels a and b respectively) for a typical irradiation of a CO:H_2O ice. The bi-exponential model provides a superior fit, with a higher R^2 value of 0.998 compared to 0.987 for the single-exponential model. This difference is also evident visually, where the green trace (single-exponential) deviates more from the data than the blue trace (bi-exponential). To confirm this, Figures S8c and d show the residuals of each function plotted against irradiation time. These show that for a single-exponential fit, there is a correlated deviation at early irradiation times, which indicates that it does not capture the initial data points well. The bi-exponential fit reduces this, with residuals that are more randomly distributed around zero at early irradiation times, which is consistent with an improved description of the data.

Table S2: Details of individual irradiation experiments for CO:H_2O and N_2:H_2O mixed ices at 3 and 12 μm including; irradiation energies, bi-exponential fit parameters, time constants τ (scaled using the duty cycle *D*), and the rate constants *k* for fast and slow photon-induced desorption processes.

Ice configuration, X:H_2O	Irradiation wavelength, λ_{FEL}	Irradiation energy, E_{FEL}	I_1	I_2	I_1/I_2	I_∞	Time constants, τ_i*D		Rate constants, k	
X	**λ_{FEL} / μm**	**E_{FEL} / 10^{-2} J**	**/ 10^3**	**/ 10^3**		**/ 10^3**	**τ_1 / 10^{-8} s**	**τ_2 / 10^{-8} s**	**k_1 / 10^7 s^{-1}**	**k_2 / 10^7 s^{-1}**
CO	3.1	3.97 ± 0.50	970.6 ± 4.1	119.3 ± 3.3	8.14	6.7 ± 0.09	1.27 ± 0.02	17.51 ± 0.52	7.90 ± 0.11	0.57 ± 0.02
	3.0	3.60 ± 0.50	370.4 ± 1.8	53.0 ± 1.5	6.98	5.1 ± 0.05	0.85 ± 0.02	13.01 ± 0.46	11.77 ± 0.28	0.77 ± 0.03
	3.0	2.21 ± 0.25	1160.0 ± 5.6	141.4 ± 4.8	8.20	5.3 ± 0.12	1.41 ± 0.02	29.73 ± 1.06	7.11 ± 0.09	0.34 ± 0.01
	3.0	1.45 ± 0.16	599.0 ± 2.5	54.3 ± 1.6	11.04	4.8 ± 0.09	2.05 ± 0.05	33.81 ± 1.93	4.88 ± 0.12	0.30 ± 0.02
	3.0	5.20 ± 0.50	229.6 ± 2.2	30.5 ± 1.5	7.53	4.4 ± 0.08	0.98 ± 0.03	13.28 ± 0.85	10.25 ± 0.34	0.75 ± 0.05
	12.0	12.70 ± 1.00	451.4 ± 3.8	90.7 ± 3.3	4.98	5.4 ± 0.12	2.47 ± 0.06	29.93 ± 1.11	4.04 ± 0.10	0.33 ± 0.01
	12.0	5.86 ± 0.50	24.9 ± 0.8	2.0 ± 0.6	12.66	4.8 ± 0.03	0.59 ± 0.28	27.70 ± 9.70	16.81 ± 7.86	0.36 ± 0.13
N_2	3.0	2.60 ± 0.50	1240.0 ± 3.6	175.6 ± 1.9	7.06	17.2 ± 0.13	0.93 ± 0.01	43.39 ± 6.28	10.72 ± 0.17	0.23 ± 0.03
	3.0	2.30 ± 0.50	1681.0 ± 5.2	121.1 ± 3.8	13.88	14.9 ± 0.14	1.55 ± 0.02	39.57 ± 8.67	6.44 ± 0.09	0.25 ± 0.06
	3.0	2.40 ± 0.50	1203.0 ± 5.7	184.7 ± 3.3	6.51	15.8 ± 0.19	1.18 ± 0.01	20.88 ± 0.75	8.45 ± 0.08	0.48 ± 0.02
	3.0	1.40 ± 0.60	1116.0 ± 6.5	135.3 ± 5.3	8.25	11.4 ± 0.16	1.28 ± 0.03	21.06 ± 1.28	7.82 ± 0.16	0.47 ± 0.03
	3.0	1.80 ± 0.50	1091.0 ± 7.3	101.6 ± 5.5	10.74	11.2 ± 0.18	1.34 ± 0.02	17.81 ± 0.74	7.46 ± 0.12	0.56 ± 0.02
	3.0	0.90 ± 0.20	306.4 ± 2.8	34.8 ± 2.2	8.80	10.3 ± 0.07	0.90 ± 0.04	16.60 ± 1.19	11.11 ± 0.49	0.60 ± 0.04
	12.0	10.90 ± 0.50	58.3 ± 1.7	18.5 ± 0.8	3.16	12.3 ± 0.06	0.85 ± 0.01	45.41 ± 2.67	11.74 ± 0.19	0.22 ± 0.01
	12.0	10.80 ± 0.50	53.0 ± 1.8	14.2 ± 1.4	3.72	11.4 ± 0.05	2.34 ± 0.17	26.18 ± 2.73	4.27 ± 0.31	0.38 ± 0.04

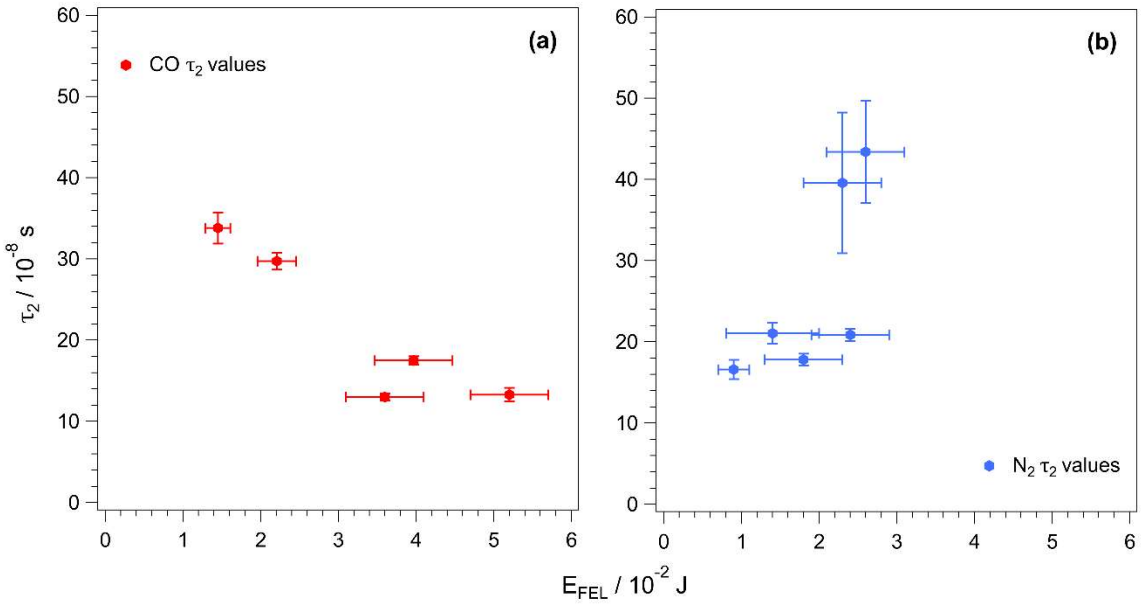

Figure S9: Plots of the τ_2 decay constants as a function of FEL energy for (a) the CO:H_2O PID experiments and (b) the N_2:H_2O PID experiments.

Figure S9 compares the τ_2 decay constants of the PID experiments as a function of FEL energy. Panel (a) shows the expected trend that increasing FEL energy causes a decrease in the decay lifetime, as explained in the main article. However, panel (b) shows what appears to be the opposite trend. This suggests that the competition between the relaxation and up-pumping rates for the N_2:H_2O system are different to that of the CO:H_2O system. This requires further investigation to be certain, and will be studied in the kinetic modelling of the ladder climbing mechanism.

References

[1] B. Rowland and J. P. Devlin, *J. Chem. Phys.*, 1991, **94**, 812–813.

[2] M. McCoustra and D. A. Williams, *Mon. Not. R. Astron. Soc.*, 1996, **279**, L53–L56.

[3] J. A. Noble, H. J. Fraser, Z. L. Smith, E. Dartois, A. C. A. Boogert, H. M. Cuppen, H. J. Dickinson, F. Dulieu, E. Egami, J. Erkal, B. M. Giuliano, B. Husquinet, T. Lamberts, B. Maté, M. K. McClure, M. E. Palumbo, T. Shimonishi, F. Sun, J. B. Bergner, W. A. Brown, P. Caselli, E. Congiu, M. N. Drozdovskaya, V. J. Herrero, S. Ioppolo, I. Jimenez-Serra, H. Linnartz, G. J. Melnick, B. A. McGuire, K. I. Oberg, G. Perotti, D. Qasim, W. R. M. Rocha and R. G. Urso, *Nat. Astron.*, 2024, **8**, 1169–1180.

[4] V. Buch and J. P. Devlin, *J. Chem. Phys.*, 1991, **94**, 4091–4092.

[5] J. He, S. Emtiaz and G. Vidali, *Astrophys. J.*, 2018, **863**, 156.

[6] M. P. Collings, J. W. Dever, H. J. Fraser and M. R. S. McCoustra, *Astrophys. Space Sci.*, 2003, **285**, 633–659.

[7] M. P. Collings, J. W. Dever, H. J. Fraser, M. R. S. McCoustra and D. A. Williams, *Astrophys. J.*, 2003, **583**, 1058–1062.

[8] J. He, A. R. Clements, S. Emtiaz, F. Toriello, R. T. Garrod and G. Vidali, *Astrophys. J.*, 2019, **878**, 94.

[9] H. J. Fraser, M. P. Collings, J. W. Dever and M. R. S. McCoustra, *Mon. Not. R. Astron. Soc.*, 2004, **353**, 59–68.

[10] M. P. Collings, J. W. Dever, H. J. Fraser and M. R. S. McCoustra, *Astrophys. Space Sci.*, 2003, **285**, 633–659.

[11] T. Zubkov, R. S. Smith, T. R. Engstrom and B. D. Kay, *J. Chem. Phys.*, 2007, **127**, 184707.

[12] E. Quirico, B. Schmitt, R. Bini and P. R. Salvi, *Planet. Space Sci.*, 1996, **44**, 973–986.

[13] M. P. Bernstein and S. A. Sandford, *Spectrochim. Acta. A. Mol. Biomol. Spectrosc.*, 1999, **55**, 2455–2466.

[14] A. L. Smith, W. E. Keller and H. L. Johnston, *Phys. Rev.*, 1950, **79**, 728.

[15] M. G. E. Van Hinsberg, M. I. M. Scheerboom and J. A. Schouten, *J. Chem. Phys.*, 1993, **99**, 752-754.

[16] T. L. Ellington and G. S. Tschumper, *Comput. Theor. Chem.*, 2013, **1021**, 109–113.

[17] S. I. Anisimov, B. L. Kapeliovich, and T. L. Perelman., *Zh. Eksp. Teor. Fiz.*, 1974, **66**, 375-377.

[18] E. Beaurepaire, J. -C. Merle, A. Daunois, and J-Y. Bigot., *Phys. Rev. Lett.*, 1996, **76**, 4250-4253.

[19] A. A. Maznev, J. A. Johnson, and K. A. Nelson., *J. Appl. Phys.*, 2011, **109**, 073517.

[20] L. Alber, V. Scalera, V. Unikandanunni, D. Schick, and S. Bonetti., *Comput. Phys. Commun.*, 2021, **265**, 107990.

[21] F. Akhmetov, N. Medvedev, I. Makhotkin, M. Ackermann, and I. Milov., *Materials*, 2022, **15**, 5193.

[22] N. Medvedev, F. Akhmetov, and I. Milov., *Int. J. Heat Mass Trans.*, 2024, **228**, 125674.

[23] D. L. Martin, *Phys. Rev.*, 1966, **141**, 576-582.

[24] P. Flubacher, A. J. Leadbetter, and J. A. Morrison., *J. Chem. Phys.*, 1960, **33**, 1751-1755.